Energy & Buildings 238 (2021) 110832

Contents lists available at ScienceDirect

Energy & Buildings

journal homepage: www.elsevier.com/locate/enb

Model predictive control optimization for rapid response and energy efficiency based on the state-space model of a radiant floor heating system

Qiong Chen [a,b], Nan Li [a,*], Wei Feng [b,*]

[a] National Centre for International Research of Low-carbon and Green Buildings, Ministry of Science & Technology, Chongqing University, Chongqing 400044, China
[b] Lawrence Berkeley National Laboratory, Berkeley, CA 94720, USA

ARTICLE INFO

Article history:
Received 15 December 2020
Revised 7 February 2021
Accepted 14 February 2021
Available online 19 February 2021

Keywords:
Model predictive control
State-space model
Energy efficiency
Response time
Radiant floor heating
Air-source heat pump

ABSTRACT

In recent years, radiant floor heating systems have been favored by more and more consumers because of their better comfort, high stability, and energy efficiency. This is especially true in southern China, where heating demand is increasing, and its application is becoming more common. This study explored the method of establishing a state-space model of a variable-flow radiant heating system without selecting and applying extensive measurement data and the application of the model predictive control method to its control optimization. The average errors between the state-space model and the experimental data in terms of the zone air temperatures and radiant floor surface temperatures were only −0.21–0.07 °C. The state-space model saves 76%~95% of the computation time compared to the Trnsys model, particularly suitable for large volumes and longtime building simulations. For the intermittent operation of the radiant floor heating with an air-source heat pump, the MPC controller reduced the response time by about 90 min compared with that with the PID controller, a reduction of approximately 56%. Besides, the MPC controller can effectively reduce energy consumption by 14.9% and improve the COP of the air-source heat pump by 24.5% compared with the PID controller.

1. Introduction

According to the latest World Energy Investment 2020 report of the International Energy Agency (IEA), global energy investment is set to decline by 20%. As a result, the situation for energy security and clean energy transition is critical, with energy supply shortages and energy transition issues particularly acute. The energy consumption of buildings dominates this picture, and a large portion of that consumption is related to heating, ventilation, and air conditioning (HVAC) systems. In recent years, radiant floor heating systems have become increasingly popular with consumers, as they provide better comfort, thermal stability, and energy efficiency. They are especially popular in southern China, where heating demand is increasing. Radiant floor heating systems can reduce the use and consumption of primary energy when they are combined with solar energy, geothermal energy, wind energy, and other renewable energy technologies, improving energy efficiency and reducing the operating costs of the radiant floor heating systems.

To study the optimal control strategy of low-temperature radiant floor heating systems, it is necessary to establish a reliable simulation model of the system. Larsen et al. [1] established a two-dimensional unsteady-state model of a low-temperature radiant floor and solved the analytical solution of the model by separating the variables. T. Weber et al. [2] believed that the star-shaped State-space model was not as complicated as the triangular network, and was only suitable for some types of enclosure structures, such as movable concrete slabs. Zhe Tian [3] and others introduced the concept of the core temperature layer of a radiant floor and established a two-dimensional unsteady heat transfer model of a concrete cooling plate. The steady-state error between the simulated value and the experimental value was within 2%, and the unsteady-state error was within 7%. Kuixing Liu [4] and others proposed a method to geometrically define the heat capacity and thermal resistance of the core temperature layer of a radiant floor. The dynamic and steady-state performance of the optimized RC model of the radiant floor were in good agreement with the finite element model. Dongliang Zhang [5] and others proposed a dynamic simplified RC model for radiant ceiling heating and underfloor ventilation (RCCUV) systems. The parameter identification by the least square method (LSM) was used to determine the thermal resistance, heat

* Corresponding authors.
E-mail addresses: nanlicqu@163.com (N. Li), weifeng@lbl.gov (W. Feng).

https://doi.org/10.1016/j.enbuild.2021.110832
0378-7788/

capacity, and convective heat transfer coefficient of the state-space model. The zone air temperature difference between the simulated and measured values was less than 0.5 K (K), and the error of heating capacity was less than 7.7%. Junke Wang [6] and others established a simplified model of a residential building and estimated all the resistance and capacity parameters based on 63 consecutive days of measured data. Zequn Wang [7] and others proposed a modeling method in which a complex initial model based on physical principles was created first, and then the model structure was simplified by gradually removing unrecognizable parameters. In the simplification process, a genetic algorithm and asymptotic confidence interval were used for parameter estimation of the model to ensure the simplified model structure maintained the sufficient fitting accuracy.

Optimizing the operation of building automation systems can greatly reduce the energy consumption of building HVAC systems. Traditional switch control, variable flow, variable water temperature, and other methods are no longer applicable, particularly for low-temperature radiant floor heating systems-the thermal characteristics of which are very different from traditional air-conditioning systems. That means that the optimal control methods should also be proposed according to specific system performance. At present, a most popular model predictive control based on a rolling optimization of the target control function is widely applied to a variety of control systems, and many research results have shown that the application of a model predictive control (MPC) to many kinds of air-conditioning systems can help those systems achieve good energy efficiency.

Feng J. et al. [8] compared the control effects of on–off control and model-based adaptive predictive control in their study. The model-based adaptive predictive control saved 25% and 55% of the energy consumption of cooling pumps and cooling towers, respectively. Schmelas M. et al. [9] proposed an adaptive predictive control system based on multiple regression. Parameter information such as outdoor air temperature, outdoor solar radiation, zone air temperature, and floor surface temperature was collected to predict the indoor heat gain at the next moment. Privara S. et al. [10] applied a model-based adaptive control system in a low-temperature radiant floor system, which saved 17%–24% of the energy consumption compared to that of the conventional control method based on outdoor temperature compensation. Pang, Xiufeng et al. [11] verified the effectiveness of an open-source MPC toolchain developed for a radiant floor system by testing. The results showed that the MPC control method reduced the system's chilled pump energy consumption by 42% and the cooling heat load by 16%. Dongliang Zhang [12] developed a simplified dynamic model of the radiant floor cooling and floor ventilation (RFCUV) system, and experimentally verified the accuracy of the model. Implementing MPC on the RFCUV system resulted in 17.5% energy savings while maintaining the same or better indoor comfort level compared to the PID controller. Li Anbang [13] established a frequency-domain state-space model for a room cooled with a low-temperature radiant floor and compared the control effects of PID control, MPC control, and offline prediction + robust feedback control through simulation. Donghun Kim [14] developed a full-order state-space model for a laboratory at Purdue University and applied the balanced truncation method to reduce the order of this linear constant model, resulting in a reduced-order model (ROM) that reduces the model's state variables by a factor of about 30 and the computational effort by a factor of three. Dong and Lam [15] introduced a control method for building heating and cooling based on the personnel-behavior model and local weather condition prediction. The experimental results showed that the energy consumption under MPC control was 30.1% lower in the heating season and 17.8% lower in the cooling season compared to the conventional temperature setting control. Donghun Kim [16] proposed an MPC algorithm for evaluating the energy-saving potential of a rooftop air conditioning unit (RTU). Simulation results showed that the MPC control method enabled the rooftop air conditioning unit to achieve energy savings of 15%–30% in most climate zones.

Jianli Chen et al.[17] applied the MPC algorithm to the hybrid ventilation systems, which maintained the thermal comfort and achieved comparative energy saving. Kui Shan et al. [18] employed the MPC algorithm to propose a direct chiller power limiting control strategy for decreasing the peak demand on the electricity. Hangxin Li [19] proposed an online multiple-objective MPC control strategy for zero energy buildings.

Most of the studies adopted a "bottom-up" approach, [20] where the wall is defined as a 3R2C model or other simplified models, and the thermal resistance and capacity of the model are mostly identified from a large amount of experimental data. The disadvantages of that approach are that bottom-up models tend to ignore the dynamic performance of the entire system and that the physical interpretation of the model is not sufficiently clear. This paper proposes the state-space model of a radiant floor heating system without extensive experimental data and gains quite excellent accuracy. The state-space model saves 76%-–95% of the computation time compared to the Trnsys model, and the MPC controller with rapid response and energy efficiency performance compared with the PID controller is validated.

The unique contributions of this research include the following:

- Development of a state-space model of a variable-flow radiant floor heating system.
- Comparison of TRNSYS and the state-space model for the low-temperature radiant floor heating system.
- Establishment of a control simulation platform for the radiant floor heating system with the air-source heat pump.
- Performance comparison of a PID controller and an MPC controller for application to the radiant floor heating system with the air-source heat pump.
- Validation of MPC controllers with rapid response and energy efficiency performance compared to PID controllers.

Besides, the second part introduces the principles of TRNSYS and state-space modeling. The third part of this paper introduces the experimental platform for the low-temperature radiant floor heating system for calibration. In the fourth part, the accuracy of the state space model is verified by comparing simulated data and experimental data. In the fifth and sixth parts, the operation results of the PID and MPC control methods are compared and investigated through simulation of the previously established models. Finally, the paper proposes the optimal control method for the radiant floor heating system suitable for residential buildings.

2. TRNSYS model and State-space model

2.1. TRNSYS model

In the TRNSYS software Due to the spacing of the pipes, a two-dimensional temperature field is created in the plane of the cross-section of the low-temperature radiant floor. The supply and return of water along the piping circuit can cause temperature changes in the piping, which affects the temperature of the floor structure in the z-direction. Therefore, a three-dimensional heat transfer model must be considered when simulating a low-temperature radiant floor system.

TRNSYS converts the triangular network structure of the core layer of the radiant floor to an equivalent star network structure, so the pipe structure can be represented by a single resistance,

Rx, meaning that the resistance of each structural element depends only on its heat transfer coefficient U value. Although the heat transfer of the radiant floor is multi-dimensional, the thermal conductivity through the upper and lower parts of the floor structure can be calculated using a one-dimensional thermal conductivity equation. Eq. (1) can be obtained after several simplifications and conversions.

$$R_x = \frac{d_x \cdot \left[In\left(\frac{d_x}{\pi \cdot \delta}\right) + \sum_{s=1}^{\infty} \frac{g_1(s)+g_2(s)}{s}\right]}{2 \cdot \pi \cdot \lambda_b} \quad (1)$$

The boundary conditions applicable to the above equation are:

$$\frac{d_i}{d_x} > 0.3 and \frac{\delta}{d_x} < 0.2$$

Therefore, the resistance *Rx* depends only on two geometric variables: (1) the distance *dx* between the pipes and the pipe diameter δ, and (2) the thermal conductivity λb of the material layer in which the pipes are located. The transition from the triangular network to the star network leads to an additional temperature ϑk at the center point of the star network, as described in detail in [21,22]. This temperature is equal to the average temperature of the layer in which the pipe is located, where y = 0 (see Fig. 1). This temperature is referred to as the core temperature.

The balanced equation for convective heat transfer in a room is shown in Eq. (2), where the left side *Qi* of the equation represents the total convective heat transfer of the air in the room, and the right side of the equation represents the sum of all convective heat transfer in the room, including the convective heat transfer between the indoor air and the inner surfaces of each enclosure $Q_{surf,i}$; the heat transfer through the cracks of doors and windows $Q_{inf,i}$; the convective heat transfer from the supplied air of the air conditioning system Q_{vent}; the convective heat transfer caused by indoor personnel, equipment, and lights $Q_{g,c,i}$; and the convective heat transfer from the adjacent areas $Q_{cplg,i}$.

$$Q_i = Q_{surf,i} + Q_{inf,i} + Q_{vent} + Q_{g,c,i} + Q_{cplg,i} \quad (2)$$

In the equation, the infiltration and ventilation volumes are determined from the amount of air exchange per unit hour in each region. Assuming that an equal amount of air leaves the room, the increased energy in area *i* due to infiltration and ventilation is shown in Eqs. (3) and (4):

$$\dot{Q}_{inf,i} = \dot{m}_{inf,i} C_p (T_a - T_i) \quad (3)$$

$$\dot{Q}_{v,i} = \sum_{k}^{nvent} \dot{m}_{v,k,i} C_p (T_{v,k} - T_i) \quad (4)$$

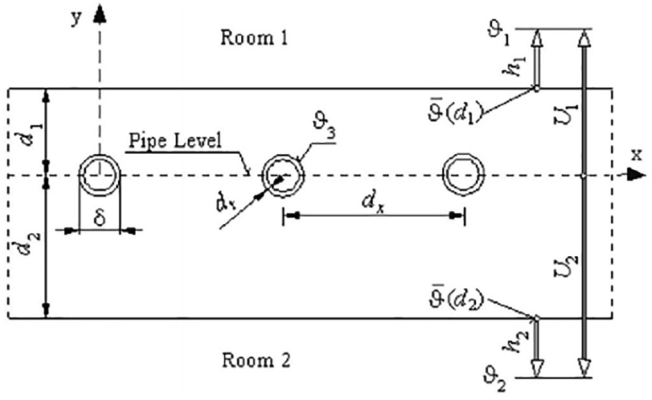

Fig. 1. The cross-section of the low-temperature radiant floor.

Where $\dot{m}_{inf,i}$ is infiltration volume, $\dot{m}_{v,k,i}$is the mass flow rate of ventilation *k*, C_p is the specific heat capacity of the air, $T_{v,k}$ is the air temperature of ventilation *k*, T_a is the ambient air temperature.

The process of radiant heat exchange on the inside surface of a window or wall in a room can be described as shown in Eq.5, where the total radiant heat gain on the inside surface of the wall (in the case of a wall) is shown on the left, and the sum of all radiant heat transfer with the inside surface of the wall is shown on the right.

$$Q_{r,wi} = Q_{g,r,i,wi} + Q_{sol,wi} + Q_{long,wi} + Q_{wall-gain} \quad (5)$$

where $Q_{r,wi}$ is the radiant heat gain at the temperature node of the interior surface of the wall, $Q_{g,r,i,wi}$ is the radiant heat transfer fraction of the indoor heat gain received by the interior surface of the wall, $Q_{sol,wi}$ is the solar radiation received by the wall through the window on the wall, $Q_{long,wi}$ is the long-wave radiant heat transfer between the wall and other interior surfaces and windows, and $Q_{wall-gain}$ is the internal radiant heat gain of a user-defined wall or window. All of the above terms are given in kilojoules per hour (kJ/h).

In addition to the coefficients of the transfer function, the heat transfer coefficient matrix of the wall should also take into account the convective heat transfer coefficients (αi, αo) on the inner and outer surfaces of the wall, and the total heat transfer coefficient of the wall should be calculated based on the convective heat transfer coefficient and the thermal conductivity of the wall U.

The long-wave radiant heat exchange between the inner surfaces of the walls and the convective heat exchange between the inner surfaces and the air node in the room are estimated approximately based on the star network structure given by Seem, [23] as shown in Fig. 2. This method uses an assumed temperature node (Tstar) to calculate the convective heat transfer between the air node and the interior surfaces of the walls, as well as the radiative heat transfer between the interior surfaces of the walls. The model shows good agreement for surface temperatures when compared to the detailed architectural model JOULOTTA, [24] developed in the research by Lund University in Sweden. However, there are significant differences with the calculation results with the single-node model using a combination of convective and radiative heat transfer coefficients (IEA Task 13 report [25]).

A two-band solar radiation model for windows was introduced that differs mainly in terms of short-wave solar radiation. The vis-

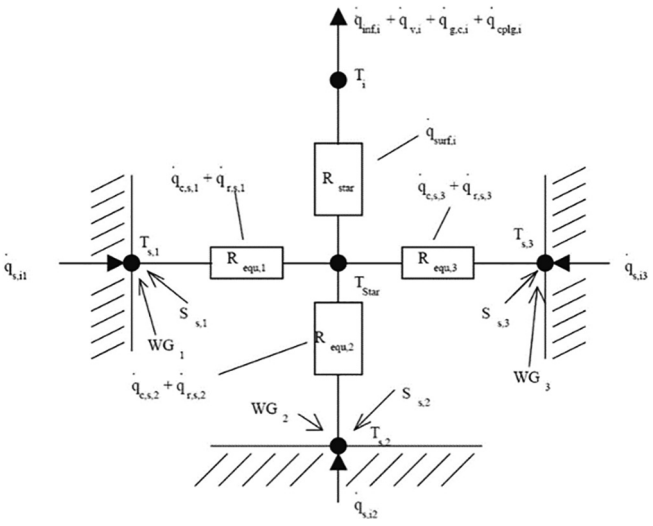

Fig. 2. The heat transfer model of a star network structure with three inner surfaces.

ible radiation can be obtained using Eq. (6). Then the invisible part of solar radiation can be calculated using Eq. (7). The model reads the visible-light transmittance and reflectance of the front and back glass layers of the window from the W4-library.

$$I_{dif,visual} = 0.466 I_{dif,solar} \tag{6}$$

$$I_{dif,non\_visual} = (1 - 0.466) I_{dif,solar} \tag{7}$$

For the calculation of the long-wave radiation exchange, it is assumed that all interior surfaces of the room are black. The heat radiated by long-wave radiation from the interior surfaces of the room is distributed according to the area ratio. Eq. (8) is used to calculate the proportion of the internal long-wave radiation absorbed by the surfaces:

$$f_{1,s} = \frac{A_s}{\sum_{surfaces} A_s} \tag{8}$$

2.2. State-space model

State-space models are dynamic time-domain models with implied time as the independent variable. State-space models not only reflect the internal state of a system but also reveal the connection between the internal state of the system and external input and output variables. This shift from variables to vectors is more suitable for modeling multiple input and output variables. The state-space model can describe the state of the system in the most careful form of present and past information, thus, it does not require large amounts of historical data, which saves time and effort.

The heat transfer process from the inner to the outer surface of the capillary pipe can be considered as a thermal conduction process through the cylinder wall. Examining a cylinder wall with internal and external diameters *do* and *di,* the problem is one-dimensional heat conduction along the pipe radius, and the thermal conductivity of the capillary pipe is constant. In steady-state conditions, the density of heat flow at different radii is inversely proportional to the radius, but the heat flow through the entire cylinder wall is constant and does not vary with the radius. The thermal resistance of heat transfer through the entire cylinder wall is defined as in Eq. (9).

$$R_r = dx * In(do/di)/2\pi\lambda_r \tag{9}$$

Since there is a temperature gradient with z-direction throughout the radiant floor, the temperature of each structural layer of the radiant floor gradually decreases along the direction of heat transfer from the layer where the capillary is located. However, the results of the cross-sectional temperature distribution of the radiant floor based on FEM simulations show the existence of a core temperature layer near the buried pipe layer, in which the temperature is almost constant at the temperature Tc. The resistance to thermal conductivity from the outside surface of the pipe to the core temperature layer Tc is expressed by Rx. Rx is considered to be determined geometrically, and the temperature of the structural layer within 1/3*dx from the center of the capillary pipe is considered to be Tc. Based on the calculation of the thermal conductivity process, Eq. (10) can be obtained.

$$R_x = dx * (1/3) * (dx/\pi * do)/2\pi\lambda_x \tag{10}$$

At structural layers other than the core temperature layer, heat transfer can be viewed as a one-dimensional thermal conduction process along the z-direction. The structural layer above and below where the capillary pipe is located is covered with layers of backfill, decking, insulation, and flooring. To describe the dynamic thermal properties of each construction in as much detail as possible, the 2R1C network structure is used to represent the heat transfer process for each structural layer. The above-mentioned Rr, Rx, and other thermal resistors (R) and capacitances (C) are calculated based on the thermophysical properties of related materials.

A two-dimensional steady-state model of the low-temperature radiant heating floor layer has been established in many studies, assuming that the temperature in the water pipe is the average water temperature (Tw), and the temperature difference between the supply and return water is ignored. Since this study sought to investigate the optimal control strategy for radiant heating floors, it was necessary to model the heat transfer between the supply and return water along the direction of water flow in the pipes to facilitate coupling with the inlet and outlet water temperature of the air source heat pump. Rz in Fig. 3(a) represents the heat transfer resistance of the supply and return water temperature along the direction of water flow, which is calculated by Eq. (11). *Rw* represents the convective heat transfer resistance between the water with average temperature and the inner surface of the pipe, and the water flow is in the laminar state according to the flow rate inside the pipe. According to the principle of calculating the convective heat transfer coefficient in the pipe, the equation for calculating *Rw* is shown as follows. The differential equations of heat transfer of the capillary mat floor heating are shown in Eqs. (12)–(18). The dynamic state-space model of the variable-flow radiant floor is built providing the potential of its further application of variable-flow operation.

$$R_w = 1/Nu * \lambda_w * \pi * L * dx * L \tag{11}$$

$$R_z = \frac{1}{\dot{m}_{sp} \cdot c \cdot \left\{1 - exp\left[-\left(\dot{m}_{sp} \cdot c \cdot \left(R_w + R_r + R_x + \frac{1}{U_1+U_2}\right)\right)^{-1}\right]\right\}} - \left(R_w + R_r + R_x + \frac{1}{U_1 + U_2}\right) \tag{12}$$

$$C_w \frac{dT_w}{d\tau} = \frac{T_{ws} - T_w}{R_z} + \frac{T_p - T_w}{R_w} \tag{13}$$

$$C \frac{dT_{pc}}{d\tau} = \frac{T_c - T_{pc}}{R_x} + \frac{T_p - T_{pc}}{R_r} \tag{14}$$

$$C_{f4} \frac{dT_{f4}}{d\tau} = \frac{T_{s1} - T_{f4}}{R_{f7}} + \frac{T_{f3} - T_{f4}}{R_{f6} + R_{f5}} \tag{15}$$

$$C_{f3} \frac{dT_{f3}}{d\tau} = \frac{T_c - T_{f3}}{R_{f4}} + \frac{T_{f4} - T_{f3}}{R_{f6} + R_{f5}} \tag{16}$$

$$C_{f5} \frac{dT_{f5}}{d\tau} = \frac{T_c - T_{f5}}{R_{f8}} + \frac{T_{f6} - T_{f5}}{R_{f9} + R_{f10}} \tag{17}$$

$$C_{f6} \frac{dT_{f6}}{d\tau} = \frac{T_{f7} - T_{f6}}{R_{f11} + R_{f12}} + \frac{T_{f5} - T_{f6}}{R_{f9} + R_{f10}} \tag{18}$$

The state-space model of the thermal conductivity process of the wall was developed based on the thermophysical properties of the structural materials. Unlike the previous method of parameter identification to determine the values of thermal resistance R and thermal capacity C, the resistance R and capacity C for all these structural layers of the wall are determined based on parameters such as the thermal conductivity, density, specific heat capacity, and geometry of the material. Fig. 3(b) shows a simplified schematic diagram of the thermal conductive state-space model for an interior wall. The differential equations of heat transfer of the exterior walls and interior partitions are shown in Eqs. (19)–(21).

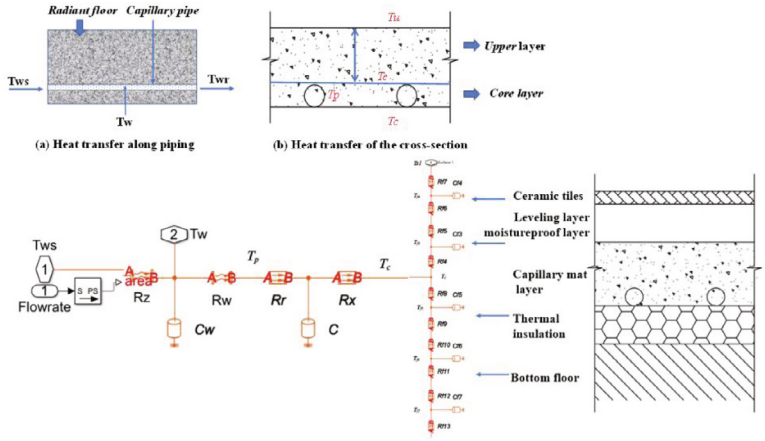

(a) The heat transfer of the capillary mat heating floor

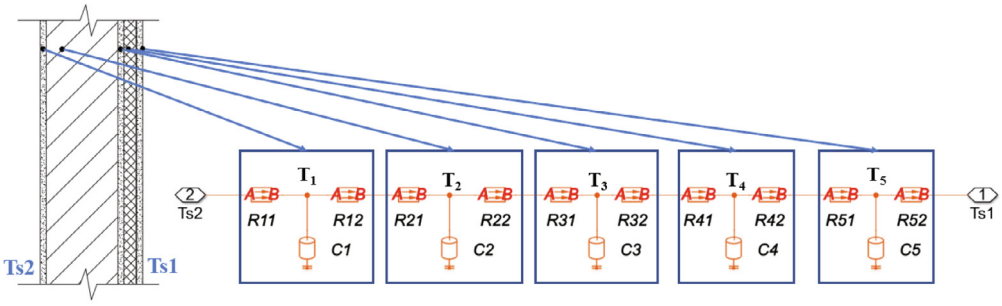

(b) The thermal conductive process through a wall

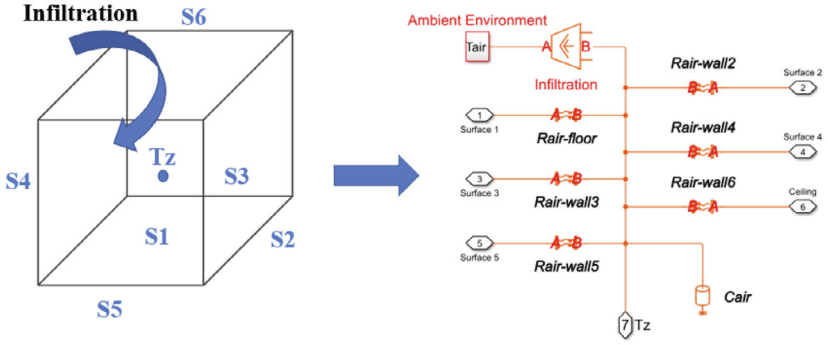

(c) Convective heat transfer process of the indoor air node

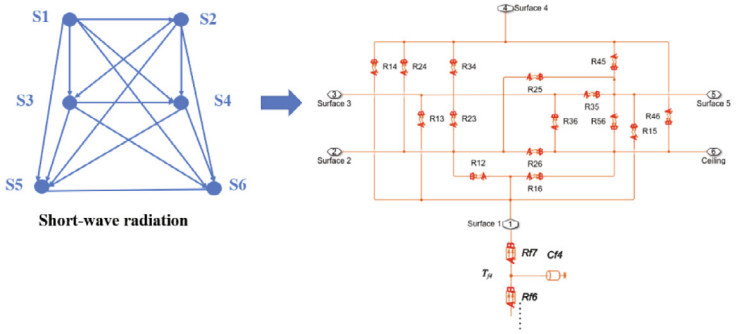

(d) The radiant transfer process among all the inner surfaces of enclosures

Fig. 3. Heat transfer process of the state-space model.

The modular state-space model of the building envelopes can greatly simplify the process of the model configuration by merely changing the wall areas with different geometry size.

$$C_1\frac{dT_1}{d\tau}=\frac{T_{s2}-T_1}{R_{11}}+\frac{T_2-T_1}{R_{12}+R_{21}} \tag{19}$$

$$C_i\frac{dT_i}{d\tau}=\frac{T_{i-1}-T_i}{R_{(i-1)2}+R_{i1}}+\frac{T_{i+1}-T_i}{R_{i2}+R_{(i+1)1}} \tag{20}$$

$$C_5\frac{dT_5}{d\tau}=\frac{T_{s1}-T_5}{R_{52}}+\frac{T_4-T_5}{R_{42}+R_{51}} \tag{21}$$

Where i = 2,3,4.

Convective heat exchange exists between the zone air and the interior surfaces of the enclosure, including floors, ceilings, and all the walls. Convective heat transfer resistor (Rc) is related to the interior surface temperature of the wall and the form of an indoor airflow organization. Based on the results of the previous study, the value of the convective heat transfer resistance between each interior surface and the zone air was determined. The state-space model for the convective heat transfer process at the zone air nodes is shown in Fig. 3(c). The calculation of the convective heat transfer through the window and door gaps was based on the number of air changes, which is illustrated in the upper part of the figure. The differential equations of heat transfer of indoor air are shown in Eq. (22).

$$C_{air}\frac{dT_{air}}{d\tau}=\frac{T_{s1}-T_{air}}{R_{air-floor}}+\frac{T_{s2}-T_{air}}{R_{air-wall2}}+\frac{T_{s3}-T_{air}}{R_{air-wall3}}+\frac{T_{s4}-T_{air}}{R_{air-wall4}}+\frac{T_{s5}-T_{air}}{R_{air-wall5}}+\frac{T_{s6}-T_{air}}{R_{air-wall6}}+q_{infiltration} \tag{22}$$

The radiant heat exchange between the floor and other interior surfaces is the dominating form of heat transfer in rooms equipped with the low-temperature radiant floor compared to conventional air conditioning. The inner surfaces of the envelopes are heated by the floor through radiant heat exchange, with each interior surface and the subsequent convective heat exchange between each interior surface and the indoor air causing the zone air temperature to rise. As opposed to most of the previous studies, in which the process of radiant heat exchange between the interior surfaces is linearized, the radiant heat transfer module in Simulink can directly characterize the heat transfer process by entering the parameters of area, angle coefficient, and Stefan Boltzmann's constant. Fig. 3(d) shows a schematic of the state-space model of radiative heat exchange between six interior surfaces of the experiment room. The differential equations of heat transfer of the envelope internal surfaces are shown in Eqs. (23)–(28). The heat transfer resistors between the envelop surfaces are linearized, and the specific linearized method refers to the research by Kim Donghun [14].

$$0=\sum_{i=2}^{6}\frac{T_{si}-T_{s1}}{R_{1i}}+\frac{T_{s2}-T_{s1}}{R_{12}}+\frac{T_{s3}-T_{s1}}{R_{13}}+\frac{T_{s4}-T_{s1}}{R_{14}}+\frac{T_{s5}-T_{s1}}{R_{15}}+\frac{T_{s6}-T_{s1}}{R_{16}}+\frac{T_{air}-T_{s1}}{R_{air-floor}}+q_{s1} \tag{23}$$

$$0=\sum_{i=3}^{6}\frac{T_{si}-T_{s2}}{R_{2i}}+\frac{T_{s1}-T_{s2}}{R_{12}}+\frac{T_{air}-T_{s2}}{R_{air-wall2}}+q_{s2} \tag{24}$$

$$0=\sum_{i=4}^{6}\frac{T_{si}-T_{s3}}{R_{3i}}+\sum_{i=1}^{2}\frac{T_{si}-T_{s3}}{R_{i3}}+\frac{T_{air}-T_{s3}}{R_{air-wall3}}+q_{s3} \tag{25}$$

$$0=\sum_{i=5}^{6}\frac{T_{si}-T_{s4}}{R_{4i}}+\sum_{i=1}^{3}\frac{T_{si}-T_{s4}}{R_{i4}}+\frac{T_{air}-T_{s4}}{R_{air-wall4}}+q_{s4} \tag{26}$$

$$0=\sum_{i=1}^{4}\frac{T_{si}-T_{s5}}{R_{i5}}+\frac{T_{s6}-T_{s5}}{R_{56}}+\frac{T_{air}-T_{s5}}{R_{air-wall5}}+q_{s5} \tag{27}$$

$$0=\sum_{i=1}^{5}\frac{T_{si}-T_{s6}}{R_{i6}}+\frac{T_{air}-T_{s6}}{R_{air-wall6}}+q_{s6} \tag{28}$$

$$\dot{x(t)}=Ax(t)+Bu(t)$$

$$\dot{y(t)}=Cx(t)+Du(t)$$

$$x=[x_1x_2x_3\cdots x_p]^T$$

$$u=[u_1u_2u_3\cdots u_n]^T$$

$$y=[y_1y_2y_3\cdots y_q]^T$$

$$A,B,C,D=f\ (R,C) \tag{29}$$

Where x(t) is the state variables, u(t) is the input variables, and y(t) is the output variables. p is the number of the state variables, n is the number of the input variables, and q is the number of the output variables. After the above differential equations of the convective and radiant heat transfer of all the building envelope surfaces and indoor air combined, the state space representation model of the radiant floor heating systems is illustrated in Eq. (29). The matrices A, B, C, D of the linear and time-invariant system are built by calculated the resistors, capacitances, and the geometry size. According to the input and state variables, the output variables of the system can be obtained.

3. The experiment platform

The experimental platform for validation was developed to calibrate the TRNSYS model and the state-space model. The plan diagram of the experimental platform is shown in Fig. 4. The experimental platform is in the form of a typical residential unit, including three bedrooms, a living room, a kitchen, and a balcony. The capillary radiant floor was installed only in the three bedrooms and the living room. The experimental platform is mainly composed of an air source heat pump, water distribution system, water pump, capillary radiant heating floor, experimental data acquisition system, and control system for the experimental platform as shown in Fig. 5.

Fig. 4. The plan diagram of the experimental platform.

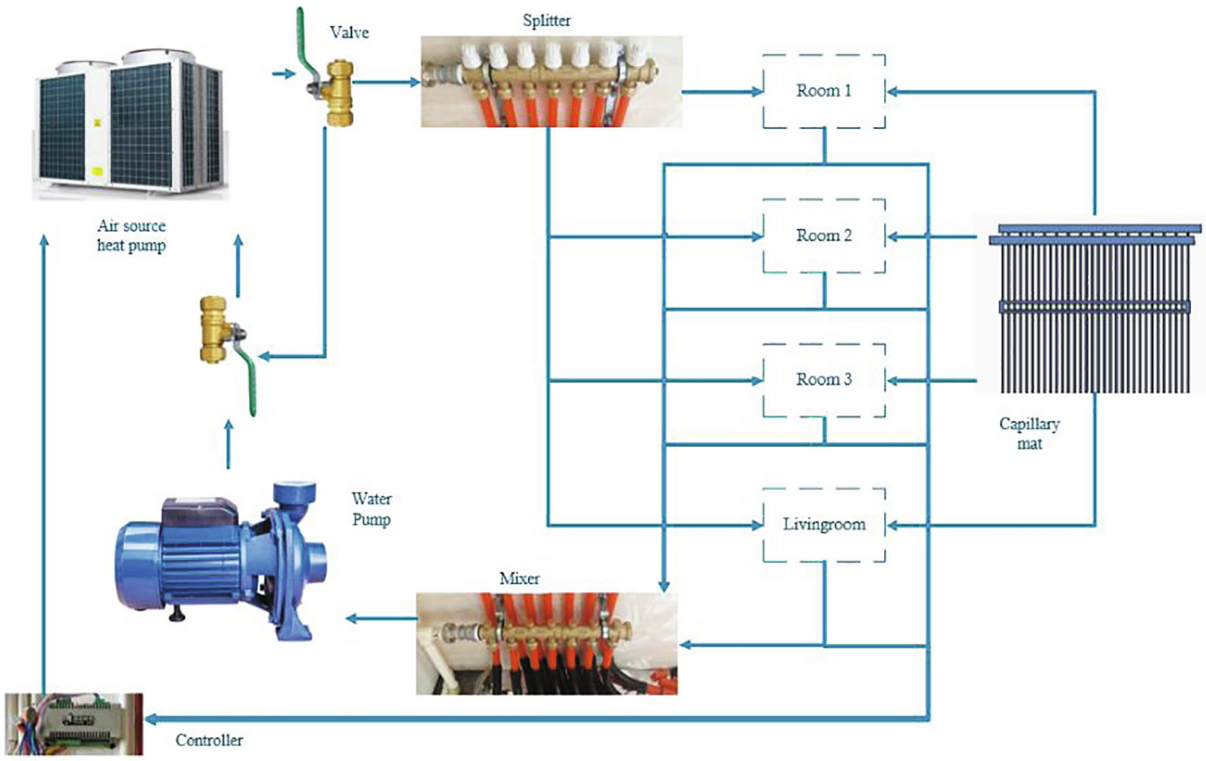

Fig. 5. The system diagram of the experimental platform.

This experimental bench is equipped with capillary modules of heat-resistant polyethylene pipe (PERT) with a diameter of 5 mm and a wall thickness of 0.9 mm. The diameter of the capillary trunk pipe is 20 mm and the wall thickness is 2 mm, according to the pipe size defined while building the state-space model of the radiant floor. Fig. 8 shows the system diagram of the experimental platform. An air-source heat pump was selected as the heat source to supply hot water to the experimental system. The water distribution system includes a water pump, a flow splitter, a flow mixer, and four electric valves that control the hot water transfer along the water pipe.

The lab bench's data acquisition system consists of T-type thermocouples, an Agilent data acquisition instrument, heat meters, a heat meter communication acquisition system, a Honeywell data monitoring system, and an outdoor weather station, among other equipment. The data acquisition system mainly collects interior wall surface temperatures, radiant floor surface temperatures, vertical zone air temperatures, water temperatures, and supplying heat. In this study, T-type thermocouples were used to measure the vertical zone temperatures and surface temperatures. The measured temperature points of the interior surfaces of walls, including walls, floors, and ceilings, are "plum-shaped". A separate temperature measurement point was placed for windows or doors. A vertical line was suspended from the ceiling of the room to measure the vertical zone air temperature gradient for calibrating the zone temperatures of the built models. The thermocouple was applied to the inner surface of the enclosure to measure the surface temperature for validating the average interior wall surface temperatures, and all the wall thermocouple probes were covered with tin foil to avoid the effect of radiant heat transfer on the accuracy of the measurement results.

During the experiments, data such as supply and return water flow rates and temperature in each room were collected as the input parameters of the radiant floor model. Real-time supply and return water temperature of the air source heat pump can be recorded through the PC-based IoT management system when networked. Instrumentation used during the experiments included ultrasonic heat meters, T-type thermocouples, and Agilent data collectors. Details are shown in Table 1.

As shown in the flow chart in Fig. 6, the experimental platform was developed and applied to calibrate the proposed models. The measurement data, including water temperature, water flow, weather data, zone temperature, and surface temperatures of the envelopes were compared with simulation data of the two models to validate the agreement between them. The control method optimization is supposed to be conducted after the successful model calibration through the simulation platform that was developed.

4. Model calibration

To verify the accuracy of the TRNSYS model and state-space model, the experimental data were compared with the simulation data of the two models under the same operational conditions. To verify the dynamic performance of the model, the setpoint of the zone air temperature in the test condition fluctuated throughout the day. When the air-source heat pump was shut down and stopped supplying heat at 8:00 a.m., the zone air temperature decreased. When the air-source heat pump ran to supply hot water

Table 1
Details of the experimental instruments.

Instrument	Model	Measuring range	Precision
Ultrasonic heat and cold meters	UHM-015	2–95 °C $0.03m^3/h \sim 3.0m^3/h$	±0.01 °C $\pm 0.001m^3/h$
T-type thermocouples	/	−40~+125 °C	±0.5 °C
Agilent data collectors	Agilent 34972A	−200~+350 °C	/

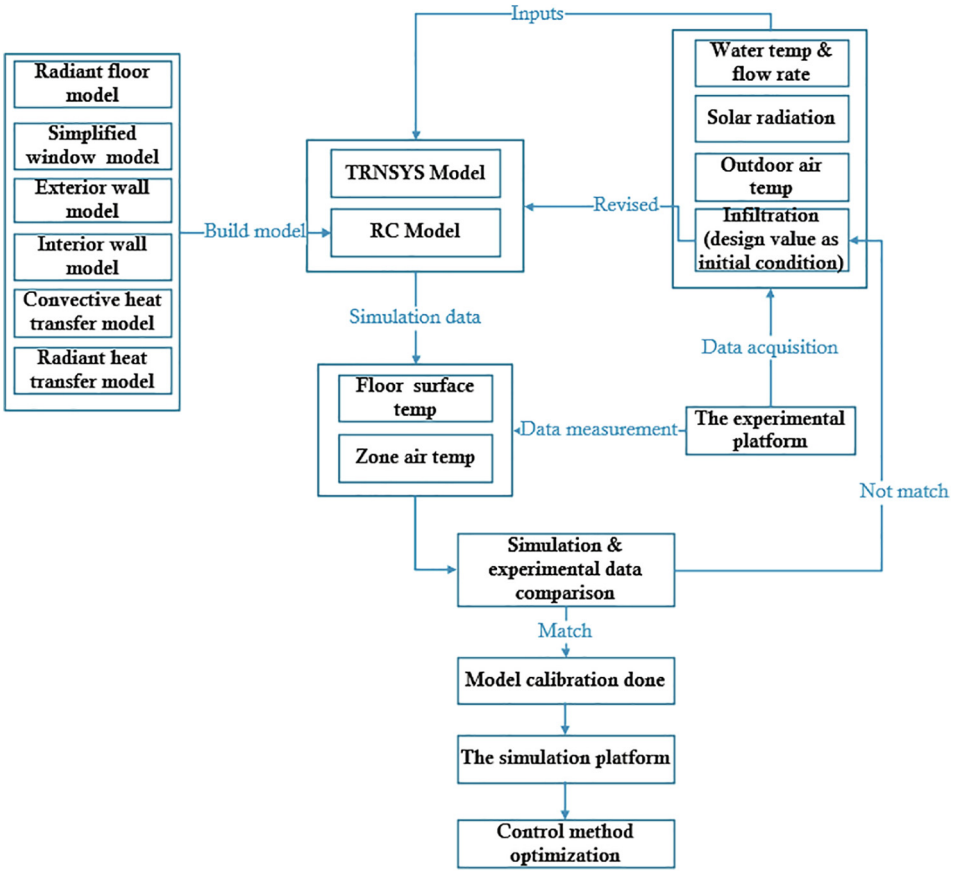

Fig. 6. The flow chart of the research.

to the radiant floor at 6:00p.m., the zone air temperature warmed. The zone air temperature was always increasing or decreasing since the thermostat has a "dead zone" where the zone air temperature fluctuates between Tset ± 0.5 °C; this provided the potential to verify the models' dynamic performance.

This study conducted a comparative analysis of two indicators—the floor surface temperature and the zone air temperature-to verify the accuracy of the models. The floor surface temperature is an indicator that directly reflects the reliability of the low-temperature radiant heating floor model, while the zone air temperature was the control target variable of the experimental system.

Fig. 7 shows a comparison of the experimental and simulated data for the floor surface temperature in the four experimental rooms. The blue line represents the experimental data, the orange line represents the simulated data from the TRNSYS model, and the green line represents the simulated data from the state-space model. The simulation results of the floor surface temperature of the four rooms were in good agreement with the experimental data because the floor surface temperature was mainly influenced by the radiant floor configuration and the temperature and flow rate of the water supply and return. Therefore, the floor surface temperature was barely influenced by other factors such as wind infiltration, solar radiation, and outdoor meteorological parameters, ensuring that the above input parameters of the floor in the model were consistent with the experimental conditions.

A comparison of the experimental and simulated data of zone air temperature in the four experimental rooms is shown in Fig. 8. In general, the experimental and simulated values of zone air temperature agreed well with each other. During the periods of 0:00–8:00 and 18:00–24:00, when the air source heat pump was in operation, the experimental and simulated data of zone air temperature were almost consistent. During the period of 8:00–18:00, when the air source heat pump was in the shutdown state, the zone air temperature started to decrease gradually, owing to the influence of outdoor meteorological parameters. A small discrepancy appeared between the experimental and simulated data due to the simplification of the radiation heat transfer model of the window, resulting in the received solar radiation load in the room being inconsistent with the experimental conditions. Also, the infiltration load through the door and window cracks was roughly estimated from the design values, which is one reason why the simulated zone air temperature deviated little from the experimental values. It should be noted that Room 2 has south orientation, so it received the most daily solar radiation compared with other rooms. Thus, the simplification of the window model caused the biggest error in the simulation of Room 2. This should be considered in future work; a more accurate window model is proposed to achieve better agreement between the experimental platform and the simulation models.

$$ERR = \sum_{k=0}^{N} (T_{trnsys/statespacemodel} - T_{experiment})/N$$

$$RMS = \sqrt{\sum_{k=0}^{N} (T_{trnsys/statespacemodel} - T_{experiment})^2/N}$$

Table 2 shows the ERR and RMS between experimental and simulated values for the floor surface temperature and the zone air temperature for the whole day. The mean errors for the floor surface temperature of the TRNSYS and state-space models were in

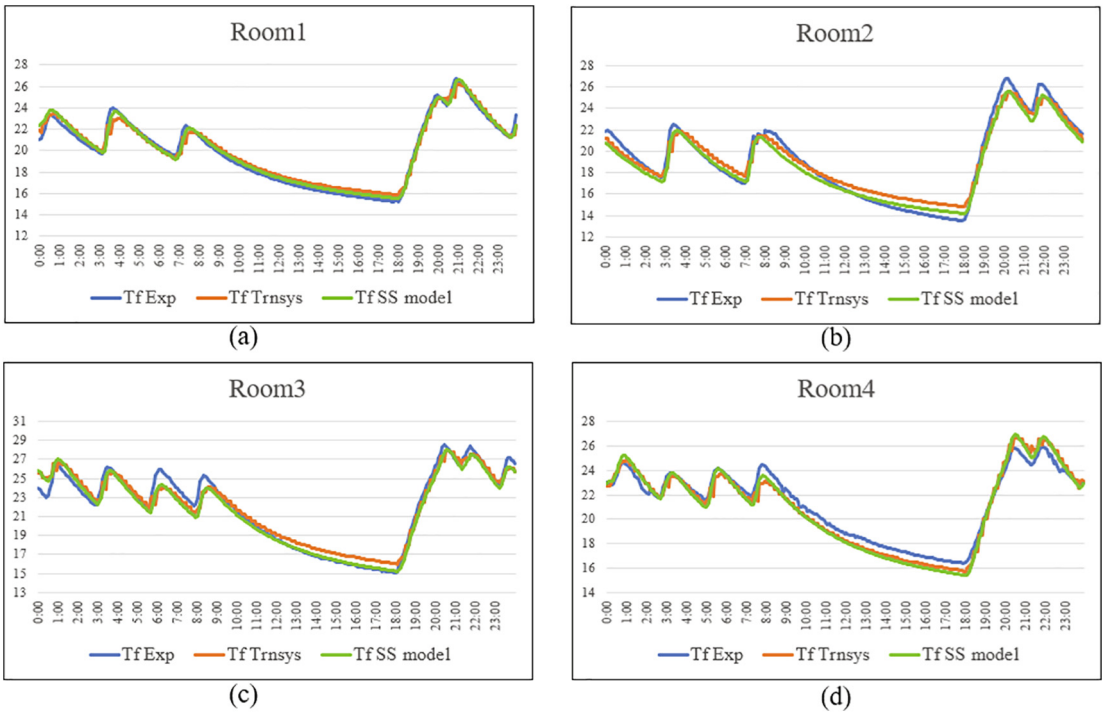

Fig. 7. Comparison of the experimental and simulated data of the floor surface temperature.

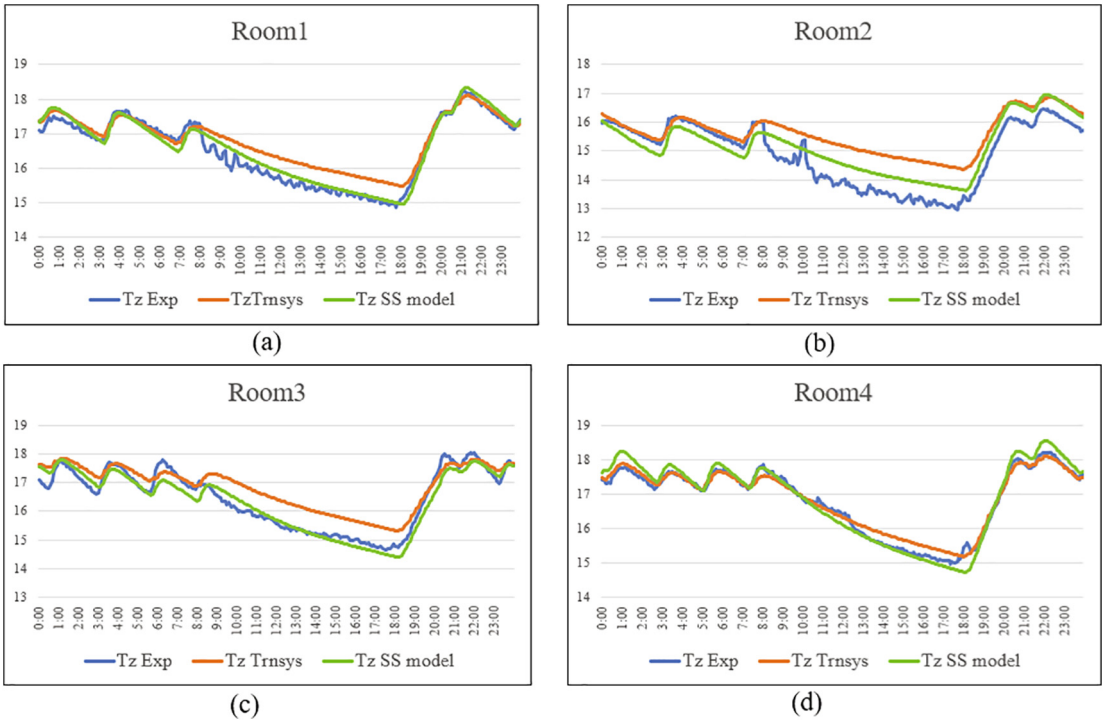

Fig. 8. Comparison of experimental and simulated data of zone air temperatures.

the range of −0.24–0.17 and −0.37–0.12, respectively. The root mean squared error was in the range of 0.53–0.84 and 0.36–0.74, respectively. The mean errors for the zone air temperature of the TRNSYS and state-space models were in the range of 0.04–0.71 and −0.09–0.26, respectively. The root mean square error was in the range of 0.16–0.89 and 0.20–0.52, respectively. The average values of ERR and RMS for the four rooms from 0:00–24:00 show that the errors of the two models are within the allowable range and that the state-space model is a little more accurate.

State-space models save a great deal of computational time compared to TRNSYS models. As shown in Table 3, the state-space model saves 76%~95% of the computation time compared

Table 2
Mean error (ERR) and root-mean-square error (RMS) for the floor surface temperature and the zone air temperature.

T_{floor}	ERR (°C)		RMS (°C)	
	Trnsys model	State-space model	Trnsys model	State-space model
Room 1	0.17	0.12	0.53	0.36
Room 2	0.08	−0.37	0.80	0.73
Room 3	0.12	−0.29	0.84	0.74
Room 4	−0.24	−0.31	0.66	0.71
Average	0.03	−0.21	0.71	0.63
T_{zone}	ERR (°C)		RMS (°C)	
	Trnsys model	State-space model	Trnsys model	State-space model
Room 1	0.26	0.07	0.39	0.20
Room 2	0.71	0.26	0.89	0.52
Room 3	0.39	−0.09	0.54	0.30
Room 4	0.04	0.04	0.16	0.22
Average	0.35	0.07	0.50	0.31

Table 3
Comparative analysis of the computational time of the state-space model and Trnsys model.

Step size	5 min		10 min		30 min	
Simulation time	30 days	365 days	30 days	365 days	30 days	365 days
State space model	1 s	5 s	1 s	3 s	0.783 s	1 s
Trnsys model	10.69 s	98.44 s	6.17 s	51.19 s	3.24 s	18.41 s
Relative ratio	−91%	−95%	−84%	−94%	−76%	−95%

to the Trnsys model, which is particularly suitable for simulating large buildings and long-term simulation.

5. Design of control systems

5.1. PID controller

As one of the earliest control algorithms developed, PID control has been used widely in industrial control systems due to its simple algorithm, great robustness, and reliability. About 90% of control systems still use a PID controller today. In simple terms, the control deviation is formed according to the given value and the actual output value and is proportional, integral, and differential by linear combination to form the output variable to adjust the controlled object.

In this study, the PID algorithm was applied to control the supply water temperature of the air source heat pump to operate in variable heating capacity according to the real-time heat load. The supply water temperature of the air source heat pump was calculated according to Eq. (30). The controlled variable and manipulated variable are zone air temperature and supply water temperature of the air source heat pump.

The Ziegler-Nichols rule, as an empirical method of PID controller parameter tuning, aims to meet the step response of the controlled system with an overshoot of 25%. The radiant floor heating system, like most industrial control processes, can be described simply as a first-order inertial system with delay. If the time constant T, gain K, and lag time τ of the model is known, the PID parameters can be calculated using the Ziegler-Nichols tuning equation, and the specific PID parameter tuning is finished by MATLAB Simulink. The step response test of the radiant floor heating system is conducted with a simulation platform under typical working conditions. The gain constant K is 24.8, the time constant T is 12 h, and the lag time τ is 0.5 h. The schematic diagram of the PID control system is shown in Fig. 9.

$$u_{k-1} = K_p\left\{e_{k-1} - \frac{T}{T_i}\sum_{j=0}^{k-1} e_j + \frac{T_d}{T}(e_{k-1} - e_{k-2})\right\} \quad (30)$$

Where e_{k-2} e_{k-1} e_k are the difference between the zone air temperature and the zone air temperature setpoint at the *k-2 k-1* and k moment. u_{k-1} is the incremental frequency of the compressor. k is the sampling sequence where Kp = 1.16, Ti = 1 h, Td = 0.25 h, and the sampling time is 300 s.

5.2. MPC controller

Model predictive control (MPC) is an advanced class of control in which the current control action is obtained at each sampling step by solving a finite-time domain open-loop optimal control function. The current state of the system is used as the initial state of the optimal control function, and the solved optimal control sequence only performs the first control action, which is the biggest difference between it and those algorithms that use precomputed control laws. Essentially, model predictive control solves an open-loop optimal control problem, of which the idea is independent of the specific model but the implementation is model-dependent. Model predictive control normally consists of four basic components: a predictive model, feedback correction, rolling optimization, and reference trajectory. The most important part is the predictive model, which is capable of predicting the future dynamic behavior of the system. That is, it is possible to predict the output at the $k + 1$ moment based on the state of the system and the input variable at the k moment. Here, the input variable at the k moment is exactly what is used to control the output of the system at the $k + 1$ time so that it maximally approximates the expected value at the $k + 1$ moment. Hence the emphasis is on the predictive role of the model rather than the form of the model.

The MPC controller maintains the zone air temperature at the setpoint by regulating the supply water temperature of the air source heat pump. The designed MPC algorithm calculates the optimal control signal at the current moment based on the thermal characteristics of the predictive model in the Np time domain. At subsequent moments, the cycle of the above procedure continues to optimize the output control signal to achieve the stable operation of the system, which is the so-called rolling optimization process. In this study, the outdoor air temperature was assumed to be

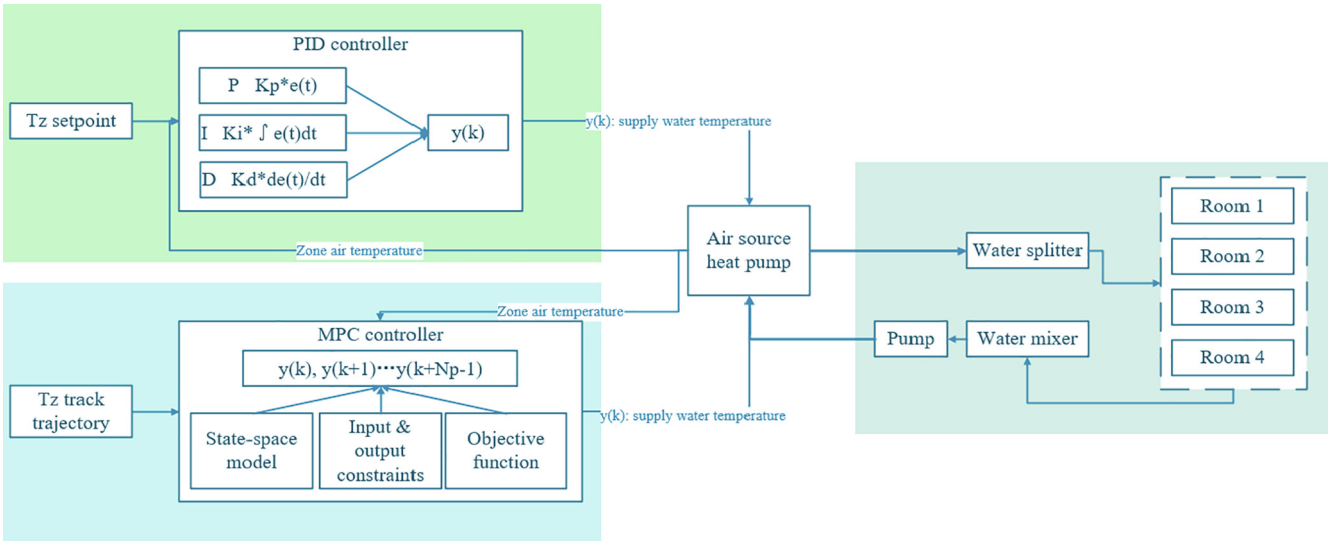

Fig. 9. The schematic diagram of the PID and MPC controller systems.

a predictor variable, while other parameters such as solar radiation and water temperature of the air source heat pump were non-monitorable variables. The optimal predicted supply water temperature of the air source heat pump at the current moment was given after the calculation of the MPC controller.

In this study, the MPC controller was designed in MATLAB. In the model identification process, the predictive model was first linearized to obtain the linearized target model. The MPC controller's target function is shown in Eq.34, where $T_{z,set}(k+i)$ is the setting value of zone air temperature at the k + i moment, and $T_z(k+i)$ is the value of zone air temperature predicted by the MPC controller at k + i moment. $u(k), u(k+1), \cdots, (k+N_p-1)$ is the calculated value of the output variables of the controller at the current k moment and the predicted output variables in the time domain Np range, which represents the supply water temperature of the air source heat pump. $\propto(i)$ and $r(i)$ denote the weights of eliminating the static difference of zone air temperature and the changing rate of the supply water temperature of the air-source heat pump, which was kept as default values 3 and 1 respectively for the achievement of the rapid response and energy efficiency.

$$x_{k+1|k} = Ax_k + Bu_k \tag{31}$$

$$x_{k+2|k} = Ax_{k+1|k} + Bu_{k+1|k} = A^2x_k + ABu_k + Bu_{k+1} \tag{32}$$

$$\begin{aligned} x_{k+Np|k} &= Ax_{k+Np-1|k} + Bu_{k+Np-1|k} \\ &= A^{Np}x_k + A^{Np-1}Bu_k + \cdots ABu_{k+Np-2} + Bu_{k+Np-1} \end{aligned} \tag{33}$$

$$\begin{aligned} J(u(k), u(k+1), \cdots, (k+N_p-1)) = \sum_{i=1}^{N_p}[\\ \propto(i)(T_{z,set}(k+i) - T_z(k+i))^2 \\ + r(i)u(k+i-1)^2] \end{aligned}$$

$$u_{min} \le u(k+i-1) \le u_{max} \tag{34}$$

The newly created scenarios were used to debug the response performance of the defined MPC controller displaying how long the zone air temperature will return to steady-state. These observable variables such as outdoor air temperature and uncontrollable variables such as solar radiation under a step or pulse input are treated as the boundary conditions. The responsive performance of the MPC controller can be tuned in the toolbox by setting the prediction horizon and control horizon. In addition, the performance of the MPC controller can be varied by adjusting the state estimation from slower to faster and the closed-loop performance from robust to aggressive, so the designed MPC controller can achieve the best operational results by applying the predictive algorithms. The schematic diagram of the MPC controller system is shown in Fig. 9.

The PID controller and MPC controller discussed above are both designed by MATLAB combined with the state-space model of the experimental rooms previously built. Then the simulation platform for the control system of the low-temperature radiant floor heating system is constructed. The state-space model of the four rooms involves a total of 365 R and 143C modules to express the heat transfer of all the envelope structures. In this study, the state-space model of a single room was chosen as the predictive model of the controller to measure the response performance of the two controllers and evaluate their advanced application to a low-temperature radiant floor heating system.

6. Results analysis

The PID and MPC controller was designed for the rapid response and energy efficiency of the radiant floor intermittent heating system with an air source heat pump. The air-source heat pump was turned off during the daytime with no people in the residential buildings, and it was turned on from 18:00 to 8:00 when the room was occupied.

The simulation results of air temperature, water supply temperature, and energy consumption of the air source heat pump for 10 days when the PID controller was running are shown in Fig. 10. And the red wireframe indicates the period of 18:00–8:00 when the heat pump was on operation, and the heat pump was turned off during the time of 8:00–18:00 when residential buildings were not occupied. As can be seen, the zone air temperature fluctuated frequently from 21.7 °C to 22.5 °C due to the large time lag characteristics of the radiant floor system. During the whole operation phase, the water temperature of the heat pump fluctuated from 35 °C to 55 °C. In the heat pump shutdown phase, the water temperature of the air source heat pump naturally cooled to a minimum of about 20 °C. The energy consumption power of the heat pump was between 3.7 and 4 kW during the heat pump operation phase.

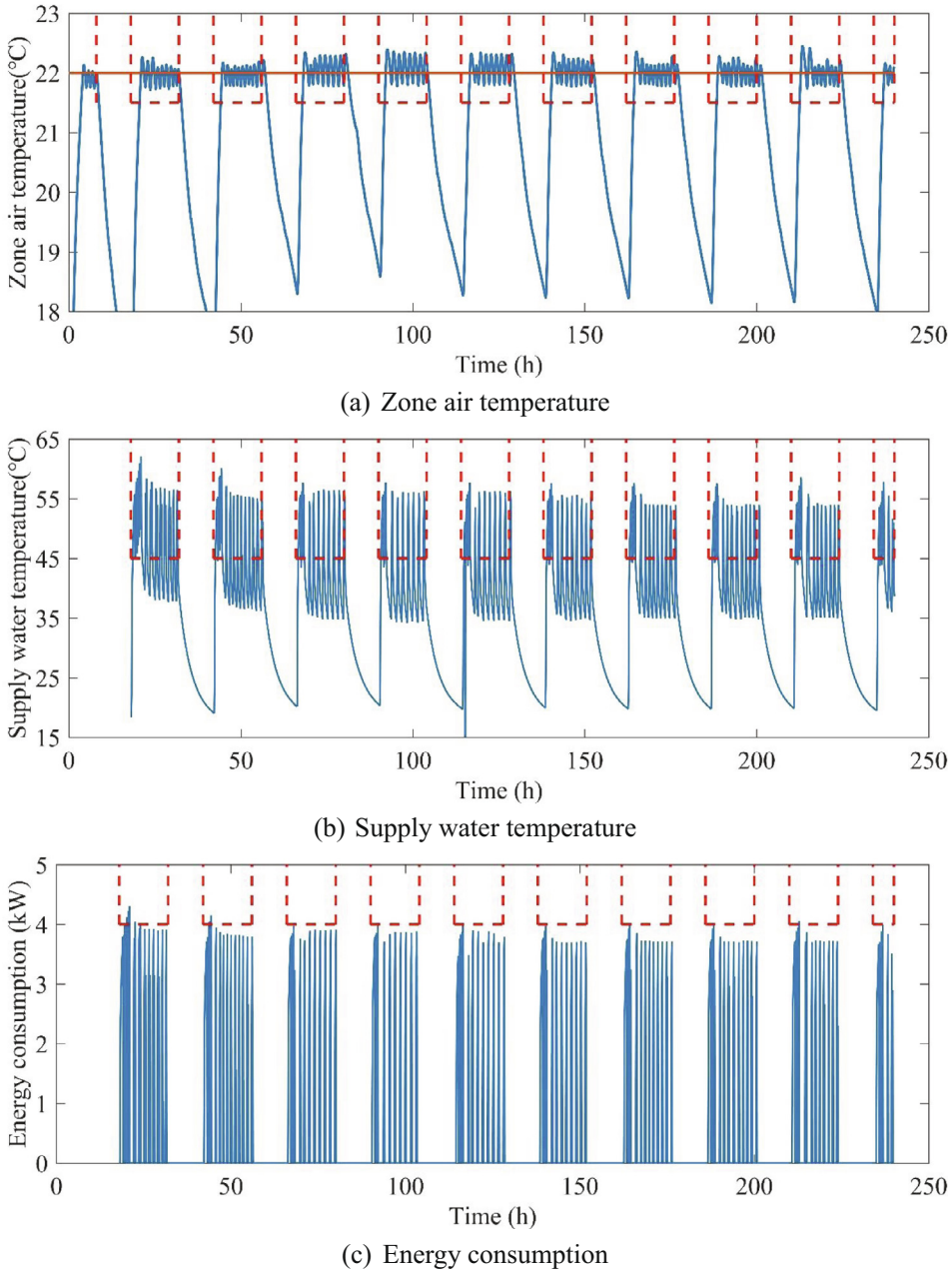

Fig. 10. Simulation results of zone air temperature, supply water temperature, and energy consumption with the PID controller in operation.

As shown in Fig. 11, the simulation results of zone air temperature, water supply temperature, and energy consumption of the air source heat pump for 10 days when the MPC controller was running. As can be seen, the zone air temperature can be stabilized at about 22 °C after the heat pump was running steadily, except when the zone air temperature reached a maximum of 22.3 °C at the start-up period of the heat pump. The water temperature of the heat pump was maintained at about 30℃ during the daytime to relieve the peak load of the heat pump when it was just turned on. During the warming response phase, the zone air temperature can reach the setpoint quickly because of the reduced heat load of the heat pump. Besides, the water temperature of the heat pump was reduced to about 35–45 °C after the system was running steadily. When the heat pump water temperature was maintained at around 30 °C, the energy consumption power of the heat pump was around 1.5 kW to 2 kW. In the stable operation phase, the heat pump can maintain the energy consumption power at around 2.8 kW operation, except for the short-time start-up period of the heat pump where the load reached up to around 3.7 kW.

In general, maintaining the water temperature of the heat pump at about 30 °C during the daytime can effectively reduce the peak load of the heat pump during the start-up phase, while greatly reducing the response time of the zone air temperature of the large time lag radiant floor system. As shown in Fig. 12, the response time of zone air temperature with the MPC controller on the operation was 70 min and that of the PID controller was 160 min. The MPC controller reduced the response time by about 90 min compared with that with the PID controller, a reduction of approximately 56%. Since the PID controller is designed for a certain operating condition, it cannot change the controller performance with the changed heat load. In contrast, the MPC controller can better adapt to the change of building load, running at high water

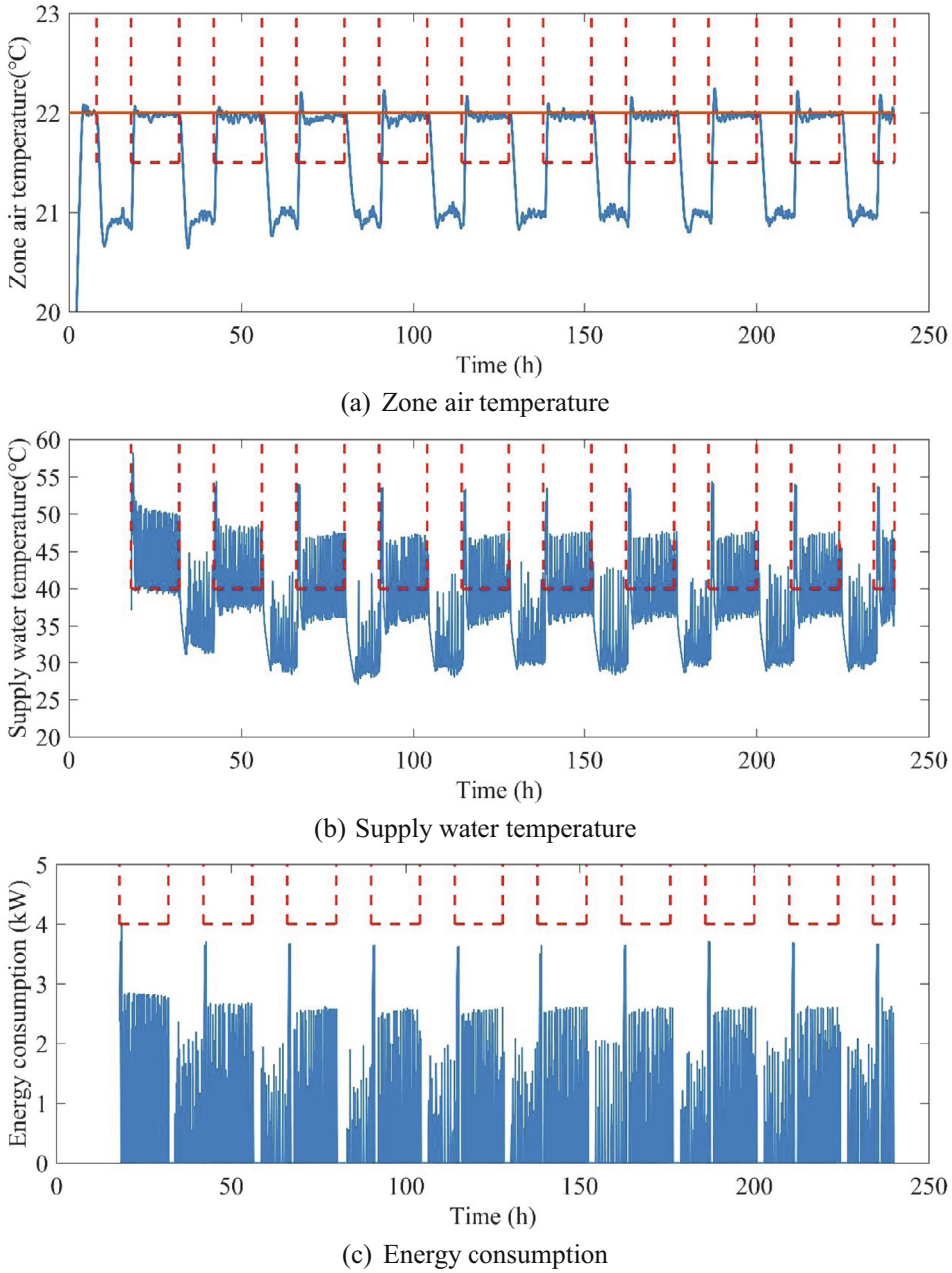

Fig. 11. Simulation results of zone air temperature, supply water temperature, and energy consumption with the MPC controller in operation.

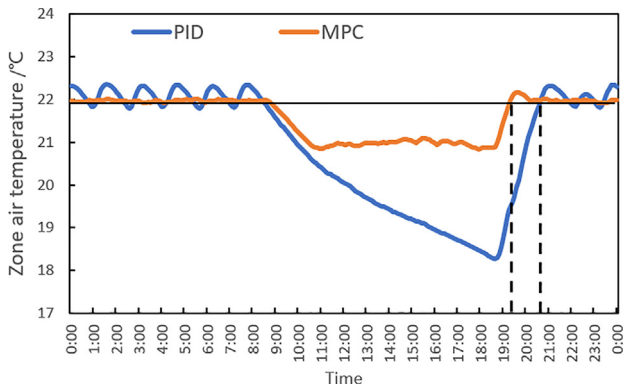

Fig. 12. Comparative results of zone air temperature with the PID controller and the MPC controller in operation.

temperature during the start-up phase to achieve rapid warming of the zone air temperature and keeping lower water temperature during the system stabilization phase, which effectively reduces the energy consumption of the heat pump. As shown in Table 4, the MPC controller can effectively reduce energy consumption by 14.9% and improve the COP of the air source heat pump by 24.5% compared with the PID controller.

Table 4
Comparison of the energy consumption, heat supply, and COP of the air-source heat pump with the PID and MPC controller in operation for 10 days.

Controller	PID	MPC	Relative percentage
Energy consumption (kWh)	134	114	−14.9%
Heat supply (kWh)	528	560	6.0%
COP	3.9	4.9	24.5%

7. Conclusion

In this study, the TRNSYS model and state-space models of an experimental platform of typical residential buildings in hot summer and cold winter zones were built. The study examined the indoor convective heat transfer process, short-wave radiant heat transfer among interior envelope surfaces, long-wave solar radiation, and complicated heat transfer model of the capillary mat radiant floors. The heat transfer processes were presented by many resistors and capacitors according to the thermal characteristics of the materials and geometry configuration. Development of the state-space model can simplify the complexity and longevity, and ensure the accuracy of the model configuration of the building envelopes without selecting and applying extensive measurement data, which provide the potential of a software framework for MPC in buildings. And the state-space model of the variable-flow radiant floor heating was proposed. The average errors between simulated and the experimental data in terms of the zone air temperatures and radiant floor surface temperatures were only −0.21~0.07 °C. The state-space model saves 76%~95% of the computation time compared to the Trnsys model, particularly suitable for large volumes and longtime building simulations. After the controlling simulation platform of the capillary radiant floor heating system was created by MATLAB, the PID and MPC algorithms were then applied to the controller of the supply water temperature of the air source heat pump to validate the model predictive control method suitable for the radiant floor heating system which has big inertial and time lag. The zone air temperature was kept at 22 °C by the MPC controller, while that of the PID controller fluctuated at 21.7 to 22.5 °C. The response time of zone air temperature with the MPC controller on the operation was reduced by about 90 min compared with that with the PID controller, a reduction of approximately 56%. The MPC controller can effectively reduce energy consumption by 14.9% and improve the COP of the air source heat pump by 24.5% compared with the PID controller, owing to the better adaptive performance of the MPC controller with the building heat load.

Declaration of Competing Interest

The authors declare that they have no known competing financial interests or personal relationships that could have appeared to influence the work reported in this paper.

References

[1] S. Flores Larsen, C. Filippín, G. Lesino, Transient simulation of a storage floor with a heating/cooling parallel pipe system, Build. Simul. 3 (2) (2010) 105–115.

[2] T. Weber, G. Jóhannesson, An optimized RC-network for thermally activated building components, Build. Environ. 40 (1) (2005) 1–14.

[3] Z. Tian, B. Duan, X. Niu, Q.i. Hu, J. Niu, Establishment and experimental validation of a dynamic heat transfer model for concrete radiant cooling slab based on reaction coefficient method, Energy Build. 82 (2014) 330–340.

[4] K. Liu, Z. Tian, C. Zhang, Y. Ding, W. Wang, Establishment and validation of modified star-type RC-network model for concrete core cooling slab, Energy Build. 43 (9) (2011) 2378–2384.

[5] D. Zhang, X. Xia, N. Cai, A dynamic simplified model of radiant ceiling cooling integrated with underfloor ventilation system, Appl. Therm. Eng. 106 (2016) 415–422.

[6] J. Wang, C.Y. Tang, M.R. Brambley, L.i. Song, Predicting home thermal dynamics using a reduced-order model and automated real-time parameter estimation, Energy Build. 198 (2019) 305–317.

[7] Z. Wang, Y. Chen, Y. Li, Development of State space model for thermal dynamic analysis of buildings through model structure simplification, Energy Build. 195 (2019) 51–67.

[8] J.(. Feng, F. Chuang, F. Borrelli, F. Bauman, Model predictive control of radiant slab systems with evaporative cooling sources, Energy Build. 87 (2015) 199–210.

[9] M.F.T. Schmelas, E. Bollin, Adaptive predictive control of thermo-active buiilding systems(TABS) based on a multiple regression algorithm, Energy Build. 103 (2015) 14–28.

[10] S. Prívara, J. Široký, L. Ferkl, J. Cigler, Model predictive control of a building heating system: The first experience, Energy Build. 43 (2-3) (2011) 564–572.

[11] X. Pang, C. Duarte, P. Haves, F. Chuang, Testing and demonstration of model predictive control applied to a radiant slab cooling system in a building test facility, Energy Build. 172 (2018) 432–441.

[12] D. Zhang, N. Cai, X. Cui, X. Xia, J. Shi, X. Huang, Experimental investigation on model predictive control of radiant floor cooling combined with underfloor ventilation system, Energy 176 (2019) 23–33.

[13] A. Li, Y. Sun, X. Xu, Development of a simplified resistance and capacitance (RC)-network model for pipe-embedded concrete radiant floors, Energy Build. 150 (2017) 353–375.

[14] D. Kim, J.E. Braun, Reduced-order building modeling for application to model-based predictive control, Proc. SimBuild (2012) 8.

[15] B. Dong, K.P. Lam, A real-time model predictive control for building heating and cooling systems based on the occupancy behavior pattern detection and local weather forecasting, Build. Simul. 7 (1) (2014) 89–106.

[16] D. Kim, J.E. Braun, Model predictive control for supervising multiple rooftop unit economizers to fully leverage free cooling energy resource, Appl. Energy 275 (2020) 115324, https://doi.org/10.1016/j.apenergy.2020.115324.

[17] J. Chen, G. Augenbroe, X. Song, Lighted-weighted model predictive control for hybrid ventilation operation based on clusters of neural network models, Autom. Constr. 89 (2018) 250–265.

[18] K. Shan, S. Wang, R. Tang, Direct chiller power limiting for peak demand limiting control in buildings – Methodology and on-site validation, Autom. Constr. 85 (2018) 333–343.

[19] H. Li, S. Wang, Model-based multi-objective predictive scheduling and real-time optimal control of energy systems in zero/low energy buildings using a game theory approach, Autom. Constr. 113 (2020) 103139, https://doi.org/10.1016/j.autcon.2020.103139.

[20] D. Kim, J.E. Braun, A general approach for generating reduced-order models for large multi-zone buildings, J. Build. Perform. Simul. 8 (6) (2015) 435–448.

[21] Markus Koschenz, B.L., EMPA, Abteilung Energiesysteme/Haustechnik, CH-8600 Dübendorf (Switzerland), Stefan Holst, TRANSSOLAR, Energietechnik GmbH, D- 70569 Stuttgart (Germany). February 2000.

[22] G.B.V.C.F. Müller, Strahlungsheizung – Theorie und Praxis, Karlsruhe (1982).

[23] Seem, J.E., "Modeling of Heat in Buildings," Ph. D. thesis, Solar Energy Laboratory, University of Wisconsin Madison. 1987.

[24] Holst, S., "Heating load of a building model in TRNSYS with different heating systems", ZAE Bayern, Abt. 4. Stuttgart, TRNSYS-User Day 1993.

[25] Voit, P., Th. Lechner, M. Schuler, "Common EC validation precedure for dynamic building simulation programs - application with TRNSYS", TRANSSOLAR GmbH, Conference of international simulation societies 94, Zürich.